

Cerebrospinal fluid as a therapeutic medium for magnetic nanoparticle transport in brain cancer hyperthermia

Essam T Abdelwahab, Ahmed A Elsawy, Abdallah A Henedy, and Sara I Abdelsalam

Citation: Chin. Phys. B, 2026, 35 (**2**): 024701. DOI: 10.1088/1674-1056/ae07ac
http://cpb.iphy.ac.cn; http://iopscience.iop.org/cpb

What follows is a list of articles you may be interested in

Influence of various shapes of nanoparticles on unsteady stagnation-point flow of Cu-H_2O nanofluid on a flat surface in a porous medium: A stability analysis

Astick Banerjee, Krishnendu Bhattacharyya, Sanat Kumar Mahato, and Ali J. Chamkha
Chin. Phys. B, 2022, 31 (**4**): 044701. DOI: 10.1088/1674-1056/ac229b

Three-dimensional flow of Powell-Eyring nanofluid with heat and mass flux boundary conditions

Tasawar Hayat, Ikram Ullah, Taseer Muhammad, Ahmed Alsaedi, Sabir Ali Shehzad
Chin. Phys. B, 2016, 25 (**7**): 074701. DOI: 10.1088/1674-1056/25/7/074701

Slip effects on streamline topologies and their bifurcations for peristaltic flows of a viscous fluid

Z. Asghar, N. Ali
Chin. Phys. B, 2014, 23 (**6**): 064701. DOI: 10.1088/1674-1056/23/6/064701

Existence of a Hartmann layer in the peristalsis of Sisko fluid

Saleem Asghar, Tayyaba Minhas, Aamir Ali
Chin. Phys. B, 2014, 23 (**5**): 054702. DOI: 10.1088/1674-1056/23/5/054702

Effects of rotation and magnetic field on nonlinear peristaltic flow of second-order fluid in an asymmetric channel through a porous medium

A. M. Abd-Alla, S. M. Abo-Dahab, H. D. El-Shahrany
Chin. Phys. B, 2013, 22 (**7**): 074702. DOI: 10.1088/1674-1056/22/7/074702

Cerebrospinal fluid as a therapeutic medium for magnetic nanoparticle transport in brain cancer hyperthermia

Essam T Abdelwahab[1,2], Ahmed A Elsawy[1], Abdallah A Henedy[1,2], and Sara I Abdelsalam[3,4,†]

[1] *Basic Engineering Sciences Department, Faculty of Engineering, Menofia University, Shebin El-Kom, Egypt*

[2] *Faculty of Engineering, Menoufia National University, Menoufia, Egypt*

[3] *Basic Science, Faculty of Engineering, The British University in Egypt, Al-Shorouk City, Cairo* 11837, *Egypt*

[4] *Instituto de Ciencias Matemáticas ICMAT, CSIC, UAM, UCM, UC3M, Madrid* 28049, *Spain*

(Received 4 April 2025; revised manuscript received 6 June 2025; accepted manuscript online 17 September 2025)

Neuronanomedicine is a promising interdisciplinary field combining two critical fields, neuroscience and nanotechnology. This study focuses on the engineering of magnetized nanoparticles (MNPs) in diagnosing and treating neurological disorders and brain cancer. Additionally, this mechanism enhances the effectiveness of magnetic-guided drug delivery. The alternating magnetic field is applied to control the directions of the MNPs to target the tumor cells. This study approaches the radiotherapy techniques of magnetic hyperthermia therapy (MHT), wherein the thermal radiative heat transfer effect is applied to achieve homogenous heating to destroy cancer cells. MNPs are injected through the cerebrospinal fluid (CSF) transport in the glymphatic system. The elastic properties of the cerebral arteries cause peristaltic propulsion for the resulting nanofluid. Therefore, the effective Maxwell model for the nanofluid thermal conductivity is selected. The nanofluid governing equations are solved using the perturbation technique under small wavelength number and long wavelength approximation with small Reynolds number. Additionally, the effects of thermal slip and elastic properties boundary conditions are incorporated. The graphical results for the streamwise velocity, pressure, and temperature distributions are plotted using MATLAB package considering the different effects of the magnetic flux intensity, thermal radiation parameter, thermal slipping at boundaries, elastic wall properties, and nanoparticle concentration. The results demonstrate the strong impact of the magnetic field and radiation heating in terms of enhancing the nanofluid CSF flow behavior and destroying cancer.

Keywords: peristaltic flow, thermal radiation, magnetic field, nanofluid, perturbation technique

PACS: 47.11.–j, 47.10.–g, 47.50.–d, 67.30.ef

DOI: 10.1088/1674-1056/ae07ac **CSTR:** 32038.14.CPB.ae07ac

1. Introduction

Brain cancer is one of the most arduous challenges in modern medicine due to its aggressive nature, high mortality rates, and limited effective therapies. Despite advances in traditional treatments such as surgery, chemotherapy, and radiation therapy, the prognosis and elimination of brain cancer continue to pose a significant challenge. This underscores the urgent need for innovative approaches to improve early detection and enhance therapeutic efficacy while minimizing systemic toxicity.[1]

Recently, neuronanoscience garnered great interest among scientists as a promising field of study. This signifies the convergence of neuroscience and nanotechnology. This field has the potential to revolutionize the diagnosis and treatment of brain cancer.[2] The brain tumor microenvironment involves complex fluid dynamics, including interstitial fluid flow, blood flow, and cerebrospinal fluid (CSF) circulation. Neuronanoscience helps study these dynamics to understand tumor growth and metastasis. It also provides innovative strategies to overcome the limitations of traditional therapeutics by utilizing the unique properties of integrated nanomaterials. The blood-brain barrier (BBB) presents a significant challenge, as it is a highly selective physiological barrier that hinders treatment by limiting the delivery of therapeutic agents to the tumor site. Nanoparticles can be engineered to open and cross the BBB, facilitating the delivery of chemotherapy drugs or gene therapeutic agents to the microenvironment of brain tumors while minimizing damage to healthy tissue. This procedure is known as targeted drug delivery to brain tumors, ensuring efficient transport and distribution of nanotherapeutics within the complex vascular and interstitial spaces of the brain.[3–5] In addition to target drug delivery, neuronanoscience also enables the development of advanced diagnostic tools, such as nanoscale imaging agents and biosensors, which can detect brain cancer at earlier stages and with greater accuracy. These innovations not only facilitate timely intervention but also provide real-time monitoring of treatment response.[6,7]

Nanofluids hold immense potential in the biomedical engineering field. Magnetic nanoparticles are dispersed through the blood flow and used in improving flow behavior and destroying tumors. The magnetic nanoparticles are smaller by

†Corresponding author. E-mail: sara.abdelsalam@bue.edu.eg

© 2026 Chinese Physical Society and IOP Publishing Ltd. All rights, including for text and data mining, AI training, and similar technologies, are reserved.

one hundred to ten thousand times in size than the tumor cells. They can also be directed by a controllable magnetic field and penetrate malignant areas while they are being exposed to thermal radiation heating, facilitating cancer elimination.[8,9]

Choi and Eastman[10] established the concept of nanofluid and its dominant properties in terms of enhancing the fluid flow and heat transfer processes. The detailed review by Kumar *et al.*[11] on nanofluids emphasized the different theoretical nanofluid models that predict the best thermal conductivity for enhancing heat transfer efficiency in various applications. They also discussed the factors that influence the thermal conductivity of nanofluids, including the base fluids' type, nanoparticle volume fraction, shape factor, size, temperature, surface charge, particle materials, nanoparticle's Brownian motion, clustering effect, nanolayer, and dispersion techniques. They concluded that higher concentrations and temperatures considerably improve thermal conductivity. Prior studies[12–15] reported that gold nanoparticles can effectively transport therapeutic agents for drug delivery. These nanoparticles exhibit strong ferromagnetic properties and high thermal conductivity. These great features made them suitable for use in photothermal and magnetic hyperthermia therapies aimed at destroying malignant cells. Additionally, these ferromagnetic gold nanoparticles were found to be safe, with no adverse chemical interactions with blood flow or other biological fluids in humans.

Magnetic hyperthermia therapy (MHT) and photothermal therapy (PTT) are emerging strategies in the management of brain tumors, particularly glioblastoma. These methods primarily depend on the leverage from oscillating magnetic field and thermal heating by radiation resulting from near-infrared laser to induce tumor cell death while minimizing damage to surrounding healthy tissue. The integration of these therapies with other modalities, such as radiotherapy, chemotherapy, and immunotherapy, boosts their effectiveness in eliminating the cancerous. PTT utilizes nanoparticles with high thermal conductivity that absorb radiation laser light and convert light to heat, effectively targeting tumors. This method can bypass drug resistance and reduce side effects on healthy tissues. MHT uses the magnetic field to direct the gold nanoparticles to the tumors accurately. This therapy involves raising tumor temperatures to induce necrosis or apoptosis. Mild hyperthermia (41 °C–45 °C) can improve the efficacy of chemotherapy and radiotherapy by enhancing the tumor microenvironment.[16–18]

Abdelsalam *et al.*[19] examined the effective role of hyperthermia therapy in treating cancer under the influence of thermal radiation and activation energy. Their study evaluated the behavior of the electroosmotic flow of Sutterby nanofluids influenced by peristaltic waves in an asymmetric channel under conditions of long wavelength (LWL) and low Reynolds numbers (LRNs). The analysis revealed that augmenting the temperature ratio parameter led to higher temperature and concentration levels within the fluid. The dimensionless reaction rate substantially enhances the kinetic energy of the reactants and the temperature field, while the magnetic Hartmann number has a resistive action against the fluid motion. Tharwat *et al.*[20] focused in their study on the injection of gold nanoparticles (AuNPs) driven by peristaltic waves into blood vessels for cancer therapy, highlighting the impact of their significant thermophysical properties on treatment outcomes. Their study investigated various factors affecting the behavior of blood flow, including heating processes, slipping conditions, gravity, and the shapes of AuNPs. The Hamilton–Crosser model was utilized to represent the thermal conductivity of the nanofluid, ensuring accurate predictions of the behavior of nanoparticles in the bloodstream. The governing equations for the incompressible non-Newtonian nanofluid were solved using a perturbation strategy with small wavenumbers and long wavelength approximation. The results collectively highlighted the potential of using AuNPs in enhancing blood flow dynamics for effective cancer treatment through photothermal therapy. Higher concentrations of AuNPs tended to resist flow motion and reduce streamwise velocity. Different shapes of AuNPs (bricks, cylinders, and platelets) were analyzed, with the brick shape showing the highest velocity profiles and temperature distributions due to its larger surface area. The temperature distribution profiles indicated that the nanofluid's temperature was highest at the core of the tube and decreased towards the boundaries. Increased heat source intensity and gravitational effects have contributed to higher temperature distributions. Magdy *et al.*[21] addressed a significant theoretical approach to enhance the effectiveness of cancer therapies using AuNPs. Their study has highlighted that these nanoparticles can effectively target and eliminate cancer cells when exposed to magnetic and heat flux fields. The research has explicitly examined the magnetohydrodynamic (MHD) peristaltic flow of nanofluids within the elastic-compliant outer walls of the annulus tube under the condition of slip and thermal effects. The approximated LWL strategy was used to solve the nonlinear governing equations. Subsequently, the results were compared with numerically finite volume and element methods, demonstrating the effectiveness of the LWL approach. The outcomes indicated that the flow velocity has increased with the slipping conditions, that higher heat sources led to elevated temperatures to kill tumors, and that the rise in magnetic strength has resisted the flow motion. Nuwairan and Souayeh[22] reported the effects of different shapes of AuNPs on the electro-magneto-hydrodynamic (EMHD) peristaltic propulsion of blood in a microchannel, including activation energy, bioconvection, radiation, and gyrotactic microorganisms. The governing equations were simplified us-

ing assumptions such as LRN, LWL, and Debye–Hückel linearization (DHL) for accurately modeling the complex interactions in the system and solved using MATLAB, specifically with the boundary value problems, that is, bvp4c function. Their study emphasized the increasing interest in AuNPs due to their great role in biomedicine, such as cancer radiotherapy, drug and gene delivery, and optical bioimaging. The results revealed that the nanoparticle volume fraction was increased with rising values of the Brownian motion parameter and activation energy. The concentration of motile microorganisms was found to decrease with the increase in temperature ratio parameters and Péclet numbers. Platelet-shaped nanoparticles exhibited the highest microorganism concentration, unlike the brick-shaped ones.

Recent related researches[23–25] discussed the significant issue of cancer treatment and the innovative approach of using directed AuNPs to target and destroy malignant tumors. These studies highlighted the urgency of this effective treatment due to its high atomic numbers, strong thermal conductivity to the heat transfer process, and great thermophysical properties, which enable heat generation when exposed to certain stimuli, such as transverse magnetic field and thermal radiation, effectively targeting and destroying cancer cells. In the investigation, different nanofluid models were considered, for instance, the Jeffrey nanofluid, the Carreau nanofluid, and the Casson nanofluid models under the impact of different thermophysical and flow parameters, such as relaxation time, various stresses (normal, axial, and shear) in blood vessels, magnetic Hartmann number, current density, variable electrical conductivity, electromagnetic parameter, thermophoresis, Brownian motion, activation energy, thermal radiation, Nusselt number, Péclet number, thermal Grashof number, bioconvection Rayleigh constant, electroosmosis, nanoparticles' shape, and nanoparticles' volume fraction. The authors presented various mathematical models based on nonlinear partial differential governing equations, which were solved using analytical and numerical methods, for instance, the Adomian decomposition method (ADM), LWL and LRN approach, lubrication approximations, and the homotopy perturbation method with the aid of MATLAB package and Mathematica software. These studies encapsulated the innovative strategy of using AuNPs in cancer treatment while addressing the complexities of blood flow and their interactions. Venugopal Reddy *et al.*[26] explained the interaction between thermophysical properties of the electroosmotic peristaltic flow of Casson fluid. These factors include wall slip, viscous dissipation, and Joule heating in the context of MHD electroosmotic peristaltic motion through a rotating asymmetric microchannel. The LWL and small Reynolds number assumptions were utilized to derive the governing equations for both momentum and energy balance. This approach simplifies the complex interactions in the fluid flow equations, allowing for analytical solutions to be obtained. The results indicated that the velocity, temperature, and heat transfer rate of the Casson fluid are positively influenced by the increase in the electroosmotic force. One significant finding was that an increase in magnetic field intensity led to a decrease in the velocity profile within the channel's core region caused by the Lorentz force. The temperature distributions were significantly enhanced by the increase in both joule heating and the Casson parameters. Given the brain's sensitivity and complexity, controlling the overheating delivery precisely is essential to avoid harming neural structures. Recent advancements in nanotechnology and magnetic field engineering resulted in the creation of magnetic nanoparticles that possess optimized heat generation properties and enhanced biocompatibility with valuable insights into temperature gradient distribution, ensuring the safety and effectiveness of magnetic hyperthermia in clinical applications.[27–29]

The primary motive force of biofluids in the human body mainly depends on pulsatile and peristaltic forces. The peristaltic motion refers to the rhythmic contraction and relaxation of muscles that propel biological fluids through tubular structures such as the intestines and the blood vessels. This wavy motion appears in CSF movement in the brain and is influenced by the elastic properties of para-arterial spaces surrounding cerebral arteries. Several recent theoretical articles[30–39] examined the peristaltic transport of biofluids through channels or tubes and their interaction with various physical parameters.

Motivated by the aforementioned investigations, this research is motivated by the urgent need to develop innovative therapies for brain cancer leveraging the unique properties of magnetized AuNPs and the dynamics of CSF. The ability of nanoparticles to cross the blood–brain barrier (BBB) highly depends on their physicochemical properties, particularly particle size and surface functionalization. It has been widely reported that nanoparticles with diameters less than 100 nm are more likely to penetrate the BBB through transcytosis mechanisms such as adsorptive-mediated or receptor-mediated transport. Smaller particles not only exhibit enhanced diffusivity but also reduce the risk of being captured by the reticuloendothelial system, thereby increasing their circulation time and accumulation in brain tissue. In addition to size, surface modification strategies play a crucial role in modulating nanoparticle interactions with biological barriers. To avoid the uptake of nanoparticles by the mononuclear phagocytic system, they should be designed for prolonged circulation in the bloodstream. This can be achieved through surface modifications that reduce recognition by immune cells. These design aspects are crucial in developing nanocarrier systems aimed at brain-targeted drug delivery, emphasizing the intersection of nanotechnology and neuropharmacology.[40,41]

The main purpose of the current study is to analyze the combined effects of varying magnetic fields and thermal radiation heat transfer on the injected magnetized gold nanoparticles through the CSF with peristalsis through a tubular artery in the brain for cancer treatment. The effective Maxwell model is selected to describe the thermal conductivity of the resulting nanofluids. The critical factors of study include thermal slipping at artery walls, brain wall elasticity and permeability at the glial layer boundaries, arterial curvature, magnetic field strength, heat source hyperthermia, radiation parameters, and AuNPs concentration. The complex governing equations representing this intricate nanofluid flow and its domain acquire mathematical simplification for the series solutions used following the perturbation strategy. This simplification follows the effective approach of LWL and LRN approximations. Consequently, the streamwise velocity, the through-flow velocity profiles, the pressure and pressure gradient distributions, the deformation of brain tissue profiles, and the temperature distribution were obtained and discussed.

2. Problem formulation

2.1. Geometry description

The geometrical construction of the undertaken model is centered around the perivascular space (PVS). The magnetized AuNPs are injected through the blood vessel contained in the PVS region. The geometry of the PVS is conceptualized as a thin annular space surrounded by impermeable elastic artery walls and the brain tissue, creating a distinct environment for the cerebrospinal nanofluid flow. The inner boundary of the PVS is defined by a permeable elastic glial wall and serves as a separator between the PVS and the brain tissue that is modeled using a linear elastic tube law. This modeling provides insights into the peristaltic deformation of the walls and the dynamics of the system, including the pressure difference effects of the nanofluid flow.[42] The external walls are exposed to transverse varying magnetic fields and varying thermal radiation for target gold nanoparticle delivery and tumor destruction in the brain artery. The PVS geometry is mapped to the glymphatic system, which features an elastic annular structure, reflecting the anatomical arrangement where CSF flows around cerebral arteries. This configuration is bounded internally by the arterial wall and externally by the permeable, compliant glial (astrocytic) layer, aligning well with observed physiological structures (as shown in Fig. 1). This model closely approximates the real PVS system and is compared with prior studies that use similar simplifications.[42,43] The nanofluid model is represented using a cylindrical coordinate system (R–Z). In this system, the Z-axis denotes the axial direction along the centerline of the tube, while the R-axis represents the radial direction. The nanofluid filling the PVS is assumed to be Newtonian and incompressible fluid with constant viscosity. In real physiological environments, CSF exhibits complex rheological behaviors under high shear rates.

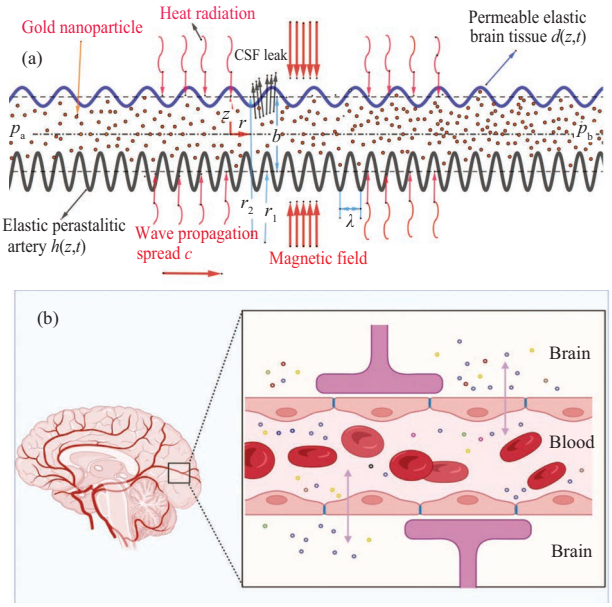


Fig. 1. Structure geometry for PVS model with elastic boundaries: (a) geometry of the problem, (b) the schematic graph for blood–brain barrier.

However, under normal conditions, CSF is generally treated as a Newtonian and incompressible fluid model, where shear rates are relatively low and non-Newtonian effects are negligible. Many research studies support the CSF as a Newtonian incompressible fluid model.[42,44–47] These studies have provided strong justification for the Newtonian approximation, where CSF has a low protein content, which is treated as water, exhibiting Newtonian and incompressible rheology. Additionally, CSF carries solute concentrations too low to alter flow; thus, the viscosity and density remain essentially identical to those of water. Normal CSF is mostly water and behaves as a Newtonian viscous fluid, meaning that in a shearing flow, the shear stress is proportional to the strain rate. In this regard, flows in the PVS are simpler to analyze than the flow of blood, which is non-Newtonian because its shearing resistance is reduced at higher strain rates as the suspended blood cells and proteins become elongated and aligned with the flow. The viscosity of normal CSF, which contains only a small amount of solutes or suspended particles, differs little from that of pure water. Therefore, when analyzing perivascular flows, we focus on the flow of an incompressible, Newtonian viscous fluid. The governing equations are simplified by LWL and LRN approximations and are subsequently solved following the procedures of perturbation methodology. The wall of peristalsis oscillates according to $h(z,t) = \hbar \sin[2\pi/\lambda(z-ct)]$, and the preamble elastic glial wall is deformed according to $d(z,t)$, where h is the imposed deformation of the traveling peristaltic wave, $\hbar$, λ, and c are the amplitude, wavelength, and velocity, respectively, z is the traveling (axial) direction, t is the time, and d represents the glial boundary deformation. The pressure

in the brain tissue is p_e, whereas p_a and p_b are assumed as pressures at the extrema of the PVS and $p_b < p_a$.

2.2. Mathematical formulation

The transformation of the unsteady frame (r, z) of the cylindrical coordinates system to the steady one (R, Z) using the same wave speed (c) requires the following method

$$R = r,\ \ Z = z - ct,\ \ U(R,Z,T) = u(r,z,t),$$
$$W(R,Z,T) = w(r,z,t),\ \ P(R,Z,T) = p(r,z,t).$$

The governing equations for the incompressible Newtonian MHD nanofluid flow with constant viscosity across the elastic PVS model are represented as follows:[42,48]

(i) Governing equations

The continuity equation:

$$\frac{1}{r}\left(\frac{\partial ru}{\partial r}\right) + \frac{\partial w}{\partial z} = 0. \tag{1}$$

The r-momentum:

$$\frac{\partial u}{\partial t} + u\frac{\partial u}{\partial r} + w\frac{\partial u}{\partial z} = -\frac{1}{\rho}\left(\frac{\partial p}{\partial r}\right) + \frac{\mu}{\rho}\left[\frac{1}{r}\left(\frac{\partial u}{\partial r}\right) + \frac{\partial^2 u}{\partial r^2} + \frac{\partial^2 u}{\partial z^2}\right]. \tag{2}$$

The z-momentum:

$$\frac{\partial w}{\partial t} + u\frac{\partial w}{\partial r} + w\frac{\partial w}{\partial z} = -\frac{1}{\rho}\left(\frac{\partial p}{\partial z}\right) + \frac{\mu}{\rho}\left[\frac{1}{r}\left(\frac{\partial w}{\partial r}\right) + \frac{\partial^2 w}{\partial r^2} + \frac{\partial^2 w}{\partial z^2}\right] - \sigma\beta_0^2 w. \tag{3}$$

The heat equation:

$$(\rho C_p)_{nf}\left[\frac{\partial T}{\partial t} + u\frac{\partial T}{\partial r} + w\frac{\partial T}{\partial z}\right] = K_{nf}\left[\frac{\partial^2 T}{\partial r^2} + \frac{1}{r}\frac{\partial T}{\partial r} + \frac{\partial^2 T}{\partial Z^2}\right] + Q_0 - \frac{1}{r}\frac{\partial}{\partial r}(rq_r). \tag{4}$$

Peristaltic deformation of the artery wall about average radii:

$$h(z,t) = \bar{h}\sin\left[\frac{2\pi}{\lambda}(z - ct)\right]. \tag{5}$$

The thermophysical properties of the nanofluid are the density, the effective dynamic viscosity, and the heat capacitance, respectively, taking the form of Ref. [49] as follows:

$$\rho_{nf} = (1-\phi)\rho_f + \phi\rho_s, \tag{6}$$
$$\mu_{nf} = \frac{\mu_f}{(1-\phi)^{2.5}}, \tag{7}$$
$$(\rho c_p)_{nf} = (1-\phi)(\rho c_p)_f + \phi(\rho c_p)_s. \tag{8}$$

The powerful Maxwell model for the thermal conductivity of the nanofluid is selected according to Ref. [50] as follows:

$$\frac{k_{nf}}{k_f} = \frac{k_p + 2k_f + 2\phi(k_p - k_f)}{k_p + 2k_f - \phi(k_p - k_f)}. \tag{9}$$

Table 1 lists the thermophysical properties of gold nanoparticles and CSF base fluids.[51] Notably, the CSF properties are approximated to agree with water properties.

Table 1. Thermophysical properties.

Thermophysical properties	CSF base fluid	Gold nanoparticles
C_p (J/kg·°C)	4180	128.8
ρ (kg/m^3)	100	19320
K (W/m·°C)	0.606	314.4

(ii) Boundary conditions

The thermal slip represents the thermal resistance at the CSF brain tissue interface due to the presence of microstructural heterogeneities at the interface, which prevents complete thermal equilibrium at the boundary. In the case of nanofluid transport, this condition reflects the influence of microscale surface effects and nanoparticle interactions at the wall, where classical no-slip assumptions for temperature gradients do not hold due to partial energy accommodation. Moreover, in biological systems, the arterial walls exhibit varying thermal conductivities due to regional vascular composition and cellular activity, further supporting the use of a thermal slip condition to capture nonideal heat transfer at the interface.[24] The glial boundary is modeled as a permeable surface to account for CSF exchange between the PVS and the surrounding brain tissue. This parameter is introduced using Darcy's law-based assumptions, which are standard for modeling flow through porous media. Wang and Olbricht[52] provided foundational estimates for fluid permeability in brain tissue and glial boundaries, which are used to define a realistic range.

No-slip boundary conditions at the peristaltic elastic artery, $r = r_1 + h$

$$w(r,z,t) = 0, \tag{10}$$
$$u(r,z,t) = \frac{\partial h(z,t)}{\partial t}. \tag{11}$$

Maximum temperature distribution at the artery wall, $r = r_1 + h$

$$\frac{\partial T}{\partial r} = 0. \tag{12}$$

Permeable boundary conditions at the elastic glial layer, $r = r_1 + b + d_0$

$$\boldsymbol{u}\cdot\boldsymbol{n} = \frac{\partial d}{\partial t} + m_e(p - p_e), \tag{13}$$

$$\boldsymbol{u}\cdot\boldsymbol{t}=0, \tag{14}$$

$$d=\frac{p-p_{\mathrm{e}}}{E_{\mathrm{e}}}. \tag{15}$$

Thermal slip at the outer wall, $r=r_1+b+d_0$

$$T-T_0=-\gamma\frac{\partial T}{\partial r}. \tag{16}$$

The pressure boundary conditions at PVS entrance $=z=0$ and PVS exit $=z=l$ under the assumption that $P_{\mathrm{b}}<P_{\mathrm{a}}$

$$p=p_{\mathrm{a}}\ \text{ at }\ z=0, \tag{17}$$

$$p=p_{\mathrm{b}}\ \text{ at }\ z=l. \tag{18}$$

Nondimensional parameters:

$$r=bR,\ \ z=\lambda Z,\ \ t=\frac{T}{\omega},\ \ u=b\omega U,\ \ w=\lambda\omega W,$$

$$p=\frac{\mu_{\mathrm{nf}}\omega}{\varepsilon^2}P,\ \ B^2=\frac{\sigma\beta_0^2b^2}{\mu_{\mathrm{nf}}},\ \ p_{\mathrm{a}}=\frac{\mu_{\mathrm{nf}}\omega}{\varepsilon^2}P_{\mathrm{a}},$$

$$p_{\mathrm{b}}=\frac{\mu_{\mathrm{nf}}\omega}{\varepsilon^2}P_{\mathrm{b}}, \tag{19}$$

$$\omega=\frac{c}{\lambda},\ \ \varepsilon=\frac{b}{\lambda},\ \ Re=\frac{\varepsilon\rho_{\mathrm{nf}}\omega b^2}{\mu},\ \ H=\frac{h}{b},$$

$$R_1=\frac{r_1}{b},\ \ R_2=\frac{r_2}{b}=R_1+1,\ \ D_0=\frac{d}{b},\ \ l=\lambda L, \tag{20}$$

$$\theta=\frac{T-T_0}{T_0},\ \ q_0=\frac{Q_0}{b\lambda\omega},\ \ \alpha_{\mathrm{nf}}=\frac{K_{\mathrm{nf}}}{(\rho C_{\mathrm{p}})_{\mathrm{nf}}}. \tag{21}$$

Applying the dimensionless analysis parameters Eqs. (18)–(20) to the governing equations (1)–(4) and their corresponding boundary conditions (6)–(13) results in the following nondimensional equations.

Nondimensional governing equations:

$$\frac{1}{R}\frac{\partial(RU)}{\partial(R)}+\frac{\partial(W)}{\partial(Z)}=0, \tag{22}$$

$$\varepsilon R_{\mathrm{e}}\left[\frac{\partial U}{\partial T}+U\frac{\partial U}{\partial R}+W\frac{\partial U}{\partial Z}\right]=-\frac{\partial P}{\partial R}+\varepsilon^2\left[\frac{1}{R}\frac{\partial U}{\partial R}+\frac{\partial^2U}{\partial R^2}+\frac{b^2}{\lambda^2}\frac{\partial^2U}{\partial Z^2}\right], \tag{23}$$

$$\varepsilon R_{\mathrm{e}}\left[\frac{\partial W}{\partial T}+U\frac{\partial W}{\partial R}+W\frac{\partial W}{\partial Z}\right]=-\frac{\partial P}{\partial Z}+\left[\frac{1}{R}\frac{\partial W}{\partial R}+\frac{\partial^2W}{\partial R^2}+\varepsilon^2\frac{\partial^2W}{\partial Z^2}\right]-\frac{\varepsilon^2\lambda^2\rho\sigma\beta}{\mu}W, \tag{24}$$

$$\frac{\varepsilon K_{\mathrm{nf}}}{\alpha_{\mathrm{nf}}K_{\mathrm{f}}}\left[U\frac{\partial\theta}{\partial R}+W\frac{\partial\theta}{\partial Z}\right]=\frac{K_{\mathrm{nf}}}{K_{\mathrm{f}}}\left[\frac{\partial^2\theta}{\partial R^2}+\frac{1}{R}\frac{\partial\theta}{\partial R}+\varepsilon^2\frac{\partial^2\theta}{\partial Z^2}\right]+\beta-R_{\mathrm{p}}\frac{1}{R}\frac{\partial}{\partial R}\left(R\frac{\partial\theta}{\partial R}\right). \tag{25}$$

Nondimensional peristaltic deformation of the artery wall about average radii:

$$H=\bar{H}\sin\left[2\pi(Z-T)\right]. \tag{26}$$

The noslip boundary conditions at $R=R_1+H$:

$$W(R,Z,T)=0, \tag{27}$$

$$U(R,Z,T)=\frac{\partial H(Z,T)}{\partial T}. \tag{28}$$

Maximum temperature distribution at the artery wall, $R=R_1+H$:

$$\frac{\partial\theta}{\partial R}=0. \tag{29}$$

Permeable boundary conditions, $R_2=R_1+1+D$:

$$\boldsymbol{V}\cdot\boldsymbol{n}=\frac{\partial D}{\partial T}+M_{\mathrm{e}}(P-P_{\mathrm{e}})\ \longrightarrow\ U=\frac{\partial D}{\partial T}+M_{\mathrm{e}}(P-P_{\mathrm{e}}), \tag{30}$$

$$\boldsymbol{V}\cdot\boldsymbol{t}=0\ \longrightarrow\ W=0, \tag{31}$$

$$\left.\begin{array}{l}\boldsymbol{V}=U\,\widehat{e_r}+W\,\widehat{e_z}\\ \boldsymbol{n}=1\,\widehat{e_r}+0\,\widehat{e_z}\\ t=0\,\widehat{e_r}+1\,\widehat{e_z}\end{array}\right\}\rightarrow, \tag{32}$$

$$D=\frac{P-P_{\mathrm{e}}}{E_{\mathrm{e}}}. \tag{33}$$

Thermal slip at the outer wall, $R_2=R_1+1+D$:

$$\theta=-\gamma\frac{\partial\theta}{\partial R}. \tag{34}$$

The pressure distribution boundary conditions at the PVS extrema (PVS entrance $=Z=0$, and PVS exit $Z=L$) under the assumption that $P_{\mathrm{b}}<P_{\mathrm{a}}$

$$P=P_{\mathrm{a}}\ \text{ at }\ Z=0, \tag{35}$$

$$P=P_{\mathrm{b}}\ \text{ at }\ Z=L, \tag{36}$$

where $\boldsymbol{V}$, $\boldsymbol{n}$, $\boldsymbol{t}\hat{e}_r$, and $\hat{e}_z$ are the flow velocity vector, normal unit vector, tangent unit vector, radial unit vector, and axial unit vector, respectively.

3. Method of solution

The perturbation methodology involves expanding the flow variables as a power series in terms of a small perturbation wavenumber ε as follows:

$$W=W_0+\varepsilon W_1+\varepsilon^2W_2+\varepsilon^3W_3+\cdots, \tag{37}$$

$$U=U_0+\varepsilon U_1+\varepsilon^2U_2+\varepsilon^3U_3+\cdots, \tag{38}$$

$$P=P_0+\varepsilon P_1+\varepsilon^2P_2+\varepsilon^3P_3+\cdots, \tag{39}$$

$$D=D_0+\varepsilon D_1+\varepsilon^2D_2+\varepsilon^3D_3+\cdots, \tag{40}$$

$$\theta=\theta_0+\varepsilon\theta_1+\varepsilon^2\theta^2+\varepsilon^3\theta_3+\cdots \tag{41}$$

After incorporating the perturbation procedures (37)–(41) into the governing equations (22)–(25) and their respective boundary conditions (26)–(34), the system analyses results in the following sets of equations.

The zero set is

$$\frac{1}{R}\frac{\partial(RU_0)}{\partial R}+\frac{\partial(W_0)}{\partial Z}=0, \tag{42}$$

$$-\frac{\partial P_0}{\partial R}=0, \tag{43}$$

$$-\frac{\partial P_0}{\partial Z}+\frac{1}{R}\frac{\partial W_0}{\partial R}+\frac{\partial^2 W_0}{\partial R^2}-\frac{b^2\rho\sigma\beta^2}{\mu}W_0=0, \tag{44}$$

$$\frac{K_{\rm nf}}{K_{\rm f}}\left[\frac{\partial^2\theta_0}{\partial R^2}+\frac{1}{R}\frac{\partial\theta_0}{\partial R}\right]+\beta-R_{\rm p}\left[\frac{1}{R}\frac{\partial\theta_0}{\partial R}+\frac{\partial^2\theta_0}{\partial R^2}\right]=0. \tag{45}$$

Boundary conditions at $R=R_1+H$

$$W_0(R,Z,T)=0, \tag{46}$$

$$U_0(R,Z,T)=\frac{\partial H(Z,T)}{\partial T}, \tag{47}$$

$$\frac{\partial\theta_0}{\partial R}=0. \tag{48}$$

Boundary conditions at $R_2=R_1+1+D_0$

$$W_0=0, \tag{49}$$

$$U_0=\frac{\partial D_0}{\partial T}+M_{\rm e}\left(P_0-P_{\rm e}\right), \tag{50}$$

$$\theta_0=-\gamma\frac{\partial\theta_0}{\partial R}. \tag{51}$$

The first set is

$$\frac{1}{R}\frac{\partial(RU_1)}{\partial R}+\frac{\partial(W_1)}{\partial Z}=0, \tag{52}$$

$$-\frac{\partial P_1}{\partial R}=0, \tag{53}$$

$$R_{\rm e}\left[\frac{\partial W_0}{\partial T}+U_0\frac{\partial W_0}{\partial R}+W_0\frac{\partial W_0}{\partial Z}\right]=-\frac{\partial P_1}{\partial Z}+\left[\frac{1}{R}\frac{\partial W_1}{\partial R}+\frac{\partial^2 W_1}{\partial R^2}\right], \tag{54}$$

$$\frac{K_{\rm nf}}{\alpha_{\rm nf}K_{\rm f}}\left[U_1\frac{\partial\theta_1}{\partial R}+W_1\frac{\partial\theta_1}{\partial Z}\right]=\frac{K_{\rm nf}}{K_{\rm f}}\left[\frac{\partial^2\theta_1}{\partial R^2}+\frac{1}{R}\frac{\partial\theta_1}{\partial R}\right]+\beta-R_{\rm p}\left[\frac{1}{R}\frac{\partial\theta_1}{\partial R}+\frac{\partial^2\theta_1}{\partial R^2}\right]. \tag{55}$$

The boundary conditions at $R=R_1+H$ are expressed as follows:

$$W_1(R,Z,T)=0, \tag{56}$$

$$U_1(R,Z,T)=0, \tag{57}$$

$$\frac{\partial\theta_1}{\partial R}=0. \tag{58}$$

The boundary conditions at $R_2=R_1+1+D_1$ is

$$W_1=0, \tag{59}$$

$$U_1=\frac{\partial D_1}{\partial T}+M_{\rm e}\left(P_1\right), \tag{60}$$

$$\theta_1=-\gamma\frac{\partial\theta_1}{\partial R}. \tag{61}$$

The second set is

$$\frac{1}{R}\frac{\partial(RU_2)}{\partial R}+\frac{\partial(W_2)}{\partial Z}=0, \tag{62}$$

$$R_{\rm e}\left[\frac{\partial U_0}{\partial T}+U_0\frac{\partial U_0}{\partial R}+W_0\frac{\partial U_0}{\partial Z}\right]=-\frac{\partial P_2}{\partial R}+\left[\frac{1}{R}\frac{\partial U_0}{\partial R}+\frac{\partial^2 U_0}{\partial R^2}\right], \tag{63}$$

$$R_{\rm e}\left[\frac{\partial W_1}{\partial T}+U_0\frac{\partial W_1}{\partial R}+U_1\frac{\partial W_0}{\partial R}+W_0\frac{\partial W_1}{\partial Z}+W_1\frac{\partial W_0}{\partial Z}\right]=-\frac{\partial P_2}{\partial Z}+\left[\frac{1}{R}\frac{\partial W_2}{\partial R}+\frac{\partial^2 W_2}{\partial R^2}+\frac{\partial^2 W_0}{\partial Z^2}\right], \tag{64}$$

$$\frac{K_{\rm nf}}{\alpha_{\rm nf}K_{\rm f}}\left[U_2\frac{\partial\theta_2}{\partial R}+W_2\frac{\partial\theta_2}{\partial Z}\right]=\frac{K_{\rm nf}}{K_{\rm f}}\left[\frac{\partial^2\theta_2}{\partial R^2}+\frac{1}{R}\frac{\partial\theta_2}{\partial R}+\frac{\partial^2\theta_0}{\partial Z^2}\right]+\beta-R_{\rm p}\left[\frac{1}{R}\frac{\partial\theta_2}{\partial R}+\frac{\partial^2\theta_2}{\partial R^2}\right]. \tag{65}$$

Boundary conditions at $R=R_1+H$

$$W_2(R,Z,T)=0, \tag{66}$$

$$U_2(R,Z,T)=0, \tag{67}$$

$$\frac{\partial\theta_2}{\partial R}=0. \tag{68}$$

Boundary conditions at $R_2=R_1+1+D_2$

$$W_2=0, \tag{69}$$

$$U_2=\frac{\partial D_2}{\partial T}+M_{\rm e}\left(P_2\right), \tag{70}$$

$$\theta_2=-\gamma\frac{\partial\theta_2}{\partial R}. \tag{71}$$

The perturbation technique primarily relies on expanding a power series solution, where the zero-order solution already captures the dominant behavior of the flow and thermophysical field. The first- and second-order terms produce minor quantitative refinements without altering the qualitative trend. Furthermore, the complexity of including second-order or higher terms was not warrante, as their contribution to the physi-

cal quantities of interest (velocity, pressure, and temperature distributions) was minima. This aligns with standard practice in low Reynolds number and long-wavelength approximation, where higher-order perturbation effects become asymptotically small and do not significantly impact the accuracy of the results, as also noted in prior studies.[1,20] Thus, for simplicity, the zero-order solution suffices for convergence, while the first and second sets are complex, with their values not significantly affecting the results. The solutions of the velocity, pressure, and temperature distributions are as follows:

$$\theta(r) = C_1 \ln(r) + C_2 + D_5 r^2, \tag{72}$$

$$W(r) = C_3 I_0\left(\sqrt{\frac{\mu_{\rm f}}{\mu_{\rm nf}}} B r\right) + C_2 K_0\left(\sqrt{\frac{\mu_{\rm f}}{\mu_{\rm nf}}} B r\right) + f(r), \tag{73}$$

$$U(r) = \frac{\partial C_4}{\partial Z}\frac{K_1\left(\sqrt{(\mu_{\rm f}/\mu_{\rm nf})B}\, r\right)}{D_1} - \frac{\partial C_3}{\partial Z}\frac{I_1\left(\sqrt{(\mu_{\rm f}/\mu_{\rm nf})B}\, r\right)}{D_1} + \frac{R}{2B}\frac{\partial^2 P_0}{\partial Z^2} + \frac{C_5}{r}, \tag{74}$$

$$P_0(z) = C_6 \exp\left(\sqrt{\frac{A_1}{A_0}} Z\right) + C_7 \exp\left(-\sqrt{\frac{A_1}{A_0}} Z\right) - \frac{A_2}{A_1}, \tag{75}$$

$$\frac{\partial P_0}{\partial Z} = C_6 \sqrt{\frac{A_1}{A_0}} \exp\left(\sqrt{\frac{A_1}{A_0}} Z\right) - C_7 \sqrt{\frac{A_1}{A_0}} \exp\left(-\sqrt{\frac{A_1}{A_0}} Z\right), \tag{76}$$

where

$$D_5 = \frac{\beta}{4\left(R_{\rm p} - \dfrac{K_{\rm nf}}{K_{\rm f}}\right)}, \tag{77}$$

$$D_6 = \frac{\left[\dfrac{I_0\left(\sqrt{(\mu_{\rm f}/\mu_{\rm nf})B}\, r_2\right)}{I_0\left(\sqrt{(\mu_{\rm f}/\mu_{\rm nf})B}\, r_1\right)} - 1\right]}{\left[K_0\left(\sqrt{(\mu_{\rm f}/\mu_{\rm nf})B}\, r_2\right) - \dfrac{I_0\left(\sqrt{(\mu_{\rm f}/\mu_{\rm nf})B}\, r_2\right)\, K_0\left(\sqrt{(\mu_{\rm f}/\mu_{\rm nf})B}\, r_1\right)}{I_0\left(\sqrt{(\mu_{\rm f}/\mu_{\rm nf})B}\, r_1\right)}\right]}, \tag{78}$$

$$C_1 = -2\, D_5 r_1^2, \tag{79}$$

$$C_2 = -\gamma\left[2 D_5 r_2 + \frac{-2 D_5 r_1^2}{r_2}\right] - D_5 r_2^2 + 2\, D_5 r_1^2 \ln(r_2), \tag{80}$$

$$C_3 = \frac{-1}{I_0\left(\sqrt{(\mu_{\rm f}/\mu_{\rm nf})B}\, r_2\right)}\left[C_4 K_0\left(\sqrt{\frac{\mu_{\rm f}}{\mu_{\rm nf}}} B r_2\right) + f(r_2)\right], \tag{81}$$

$$C_4 = \frac{1}{K_0\left(\sqrt{\dfrac{\mu_{\rm f}}{\mu_{\rm nf}}} B r_2\right) - \dfrac{K_0\left(\sqrt{\dfrac{\mu_{\rm f}}{\mu_{\rm nf}}} B r_1\right)\, I_0\left(\sqrt{\dfrac{\mu_{\rm f}}{\mu_{\rm nf}}} B r_2\right)}{I_0\left(\sqrt{\dfrac{\mu_{\rm f}}{\mu_{\rm nf}}} B r_1\right)}}\left[\frac{I_0\left(\sqrt{\dfrac{\mu_{\rm f}}{\mu_{\rm nf}}} B r_2\right)}{I_0\left(\sqrt{\dfrac{\mu_{\rm f}}{\mu_{\rm nf}}} B r_1\right)} f(r_2) - f(r_1)\right], \tag{82}$$

$$C_5 = \left[\frac{\partial C_4}{\partial Z}\frac{-r_1}{D_1} K_1\left(\sqrt{\frac{\mu_{\rm f}}{\mu_{\rm nf}}} B r_1\right) + \frac{\partial C_3}{\partial Z}\frac{r_1}{D_1} I_1\left(\sqrt{\frac{\mu_{\rm f}}{\mu_{\rm nf}}} B r_1\right) - \frac{r_1^2}{2B}\frac{\partial^2 P_0}{\partial Z^2}\right], \tag{83}$$

$$C_6 = P_{\rm a} + \frac{A_2}{A_1} - C_7, \tag{84}$$

$$C_7 = \frac{P_{\rm e} + \frac{A_2}{A_1} - \left[P_{\rm a} + \frac{A_2}{A_1}\right] \exp\left(\sqrt{\dfrac{A_1}{A_0}}(L)\right)}{\exp\left(-\sqrt{\dfrac{A_1}{A_0}}(L)\right) - \exp\left(\sqrt{\dfrac{A_1}{A_0}}(L)\right)}, \tag{85}$$

$$\frac{\partial C_4}{\partial Z} = D_6 \frac{-1}{B}\frac{\partial^2 P_0}{\partial Z^2}, \tag{86}$$

$$\frac{\partial C_3}{\partial Z} = \frac{\frac{\partial^2 P_0}{\partial Z^2}}{I_0\left(\sqrt{\frac{\mu_f}{\mu_{nf}}} B r_2\right)} \left[\frac{K_0\left(\sqrt{\frac{\mu_f}{\mu_{nf}}} B r_2\right)}{B} D_6 + \frac{1}{B} \right]. \tag{87}$$

The low Reynolds number was selected based on the high viscosity dominance created by viscous damping, compared to the low inertial effect, as indicated by the slow CSF velocities that vary between 10^{-5} m/s and 10^{-6} m/s. Then, the estimated range for R_e was $\left[5\times10^{-12} : 2\times10^{-4}\right]$. The long wavelength approximation was selected according to the short length scale for PVS width l, which ranges from 10^{-5} m to 10^{-4} m. Then, the range for long wavelength λ was estimated as [0.2:0.6], while the PVS length $(L = l/\lambda)$ was $[2 : 20]$. All other flow and geometrical parameters are indicated in Table 2 according to Refs. [42,52]. The assumptions of LWL and LRN may break down in scenarios where the flow velocity increases significantly, such as during the injection of nanoparticles into the CSF. This could lead to higher Reynolds numbers, indicating a transition from laminar to turbulent flow. This study primarily focuses on conditions where the Reynolds number is low, ensuring that inertial effects are negligible. The selected ranges for nanoparticle volume fractions, thermal source intensity, and other flow parameters are based on a combination of published experimental data and previous computational studies related to hyperthermia-based targeted therapy.[15,16] For instance, the chosen nanoparticle volume fraction values (ϕ ranging from 0.1 to 0.8) are known to provide effective heat generation. Similarly, the thermal internal heat generation source parameter β represents hyperthermia and simulates realistic heat loads delivered by magnetic or photothermal sources. Values were guided by therapeutic ranges documented in hyperthermia treatment studies, such as those by Skandalakis *et al.*[18] and Zhu *et al.*,[16] where localized tumor temperatures are elevated to 41 °C–45 °C to promote apoptosis without damaging surrounding healthy tissue.

Table 2. Estimates ranges of geometrical and flow parameters.

Parameter	Description (definition)	Estimated range
Re	Reynolds number $\left(\varepsilon\rho_n\omega b^2/\mu\right)$	$\left[5\times10^{-12} : 2\times10^{-4}\right]$
ε	perivascular film thickness (b/λ)	$\left[10^{-6} : 3.75\times10^{-2}\right]$
R_1	inner radius of the perivascular layer (r_1/b)	$\left[0.7 : 10^3\right]$
H	amplitude of the peristaltic wave $(\hbar/b)$	$\left[8\times10^{-4} : 0.5\right]$
L	perivascular length (l/λ)	$[2 : 20]$
M_e	permeability of the brain tissue $\left(k_g\mu/b\varepsilon^2\right)$	$\left[10^{-2} : 10\right]$
E_e	stiffness of the brain tissue $\left(E_g\varepsilon^2/\mu\omega\left(R_1+1\right)\right)$	$\left[2\times10^{-10} : 0.2\right]$
R_p	thermal radiation parameter $\left(\sigma^* T_0^3/k^* k_f\right)$	$[0 : 5]$

4. Results and discussion

The current investigation examines the combined influences of thermal heat radiation and magnetic field strength on the features of the dispersed magnetic AuNPs through the nanofluid flow across the glial boundary of brain tissue using a tribological model based on the first principles of the PVS. The dynamics of the enhanced nanofluid depend on the phase shift between the arterial peristaltic wave and the deformation of the glial boundary which is disrupting the flow symmetry and creating a steady stream. In order to gain thermophysical insights, the profiles of the resulting nanofluid axial velocity $W_0(r,z)$. The throughflow velocity $U_e(r,z)$, temperature distributions, pressure distribution $P_0(z)$, pressure gradient distribution $\mathrm{d}P_0/\mathrm{d}Z$, and elastic wall properties appearing in the deformation of the glial elastic layer at the boundary with brain tissue $D_0(r,z)$ are graphically represented. The graphical results are analyzed in Figs. 2–6 under the effect of sundry factors, including the magnetic field (B), heat source (β), thermal radiation parameter (R_P), thermal slip at the artery wall (γ), volume fraction of AuNPs (ϕ), brain tissue deformation (D_0) corresponding to the wall at R_2, permeability of brain tissue (M_e), stiffness of the brain tissue (E_e), pressure in the brain tissue (P_e), and inner radius of the artery (R_1).

Figures 2(a)–2(f) demonstrate the streamwise velocity profiles of the nanofluid versus radial direction under the influences of the magnetic field (B), volume fraction concentration of nanoparticles (ϕ), thermal slipping factor (γ), hyperthermia heat source intensity (β), brain tissue permeability (M_e), and the pressure at the brain tissue wall (P_e). Figure 2(a) emphasizes that the rise in Hartmann number leads to augmentation in both magnetic field strength and electrical conductivity. Therefore, this leads to an increase in the magnetic damping force, and the resistive Lorentz force appears on the nanofluid flow, ultimately resulting in a reduction in the nanofluid net velocity and flow rate for the same cross-section area. Moreover, figure 2(b) illustrates the inversely proportional effects of the volume fraction concentration of AuNPs

(ϕ) on the streamwise velocity. This is because increasing (ϕ) results in increasing the viscosity of the nanofluid due to the internal friction and leads to a loss of average kinetic energy and reducing the momentum transfer between nanofluid layers. Figure 2(c) displays that the thermal slipping factor (γ) has a proportional effect on the streamwise velocity. The rise in (γ) enhances the thermal gradient at the boundary layers and modifies boundary layer dynamics by boosting the nanofluid momentum and increasing the net axial velocity. Figure 2(d) elucidates that the augmentation in the heat source intensity (β) results in internal hyperthermia and leads to increasing the kinetic energy and, consequently, the streamwise velocity of the nanofluid. This is because of enhancing thermal buoyancy forces, which directly accelerate the fluid flow. Figure 2(e) assesses the increase in brain tissue permeability (M_e), thereby increasing the leaking of CSF at brain tissue and reducing the streamwise velocity of the nanofluid in the presence of a magnetic field. Figure 2(f) indicates the reduction in the net axial velocity as a result of increasing the pressure corresponding to the brain tissue (P_e). The increase in (P_e) compresses the glial wall toward the artery, causing the thin film thickness to decrease and restrict the flow path; thus, the nanofluid flow velocity reduces. The data corresponding to Figs. 2(a)–2(f) are tabulated in Table 3.

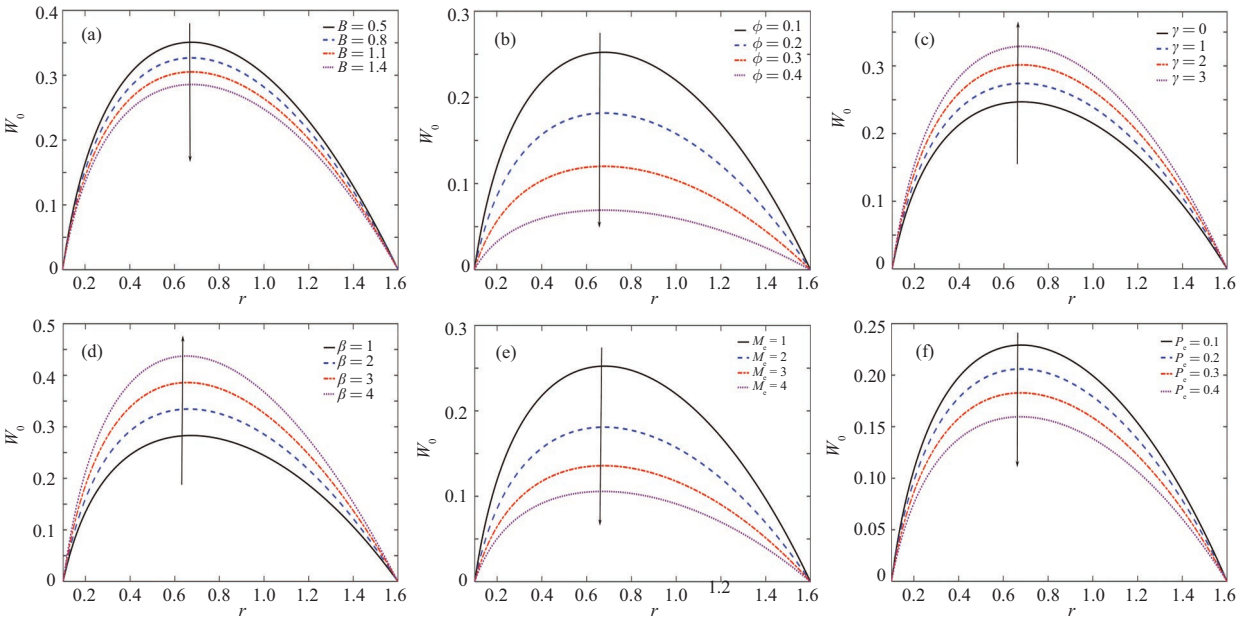


Fig. 2. The streamwise velocity distribution of the nanofluid *versus* the radial direction: (a) magnetic field strength effect, (b) the volume fraction of the gold nanoparticles effect, (c) the thermal slipping factor effect, (d) the hyperthermia heat source effect, (e) brain tissue permeability effect, and (f) the pressure of the brain tissue effect.

Table 3. Sundry emerging physical parameters corresponding to Figs. 2(a)–2(e).

Physical parameters / Figures	R_1	Z	B	ϕ	γ	β	M_e	P_e	D_0	P_a	L
Figure 2(a)	0.1	0.5	0.5 0.8 1.1 1.4	0.2	0.2	1	1	0	0.5	1	0.5
Figure 2(b)	0.1	0.5	2	0.1 0.2 0.3 0.4	0.2	1	1	0	0.5	1	0.5
Figure 2(c)	0.1	0.5	2	0.2	0.1 0.2 0.3 0.4	1	1	0	0.5	1	0.5
Figure 2(d)	0.1	0.5	2	0.2	0.2	1 2 3 4	1	0	0.5	1	0.5
Figure 2(e)	0.1	0.5	2	0.2	0.2	1	1 2 3 4	0	0.5	1	0.5
Figure 2(f)	0.1	0.5	2	0.2	0.2	1	1	0.1 0.2 0.3 0.4	0.5	1	0.5

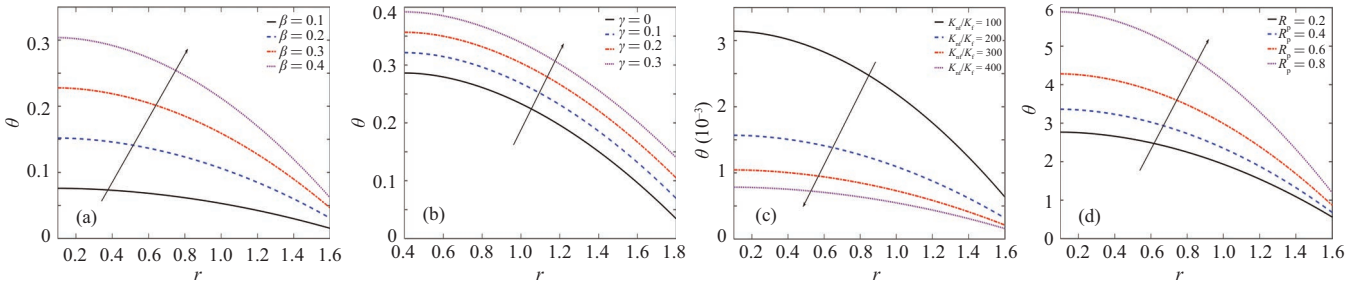


Fig. 3. The temperature distribution of the nanofluid *versus* the radial direction: (a) the heat source intensity effect, (b) the thermal slipping factor effect, (c) effective thermal conductivity of the nanofluid effect, and (d) thermal radiation parameter effect.

The temperature distributions are plotted in Figs. 3(a)–3(d) under the influences of several emerging thermophysical parameters (β, γ, $K_{\rm nf}/K_{\rm f}$, and $R_{\rm p}$). Figure 3(a) shows the directly proportional effect of internal heat generation due to high heat source intensity on the temperature profiles in the presence of thermal slipping conditions at walls. This generates useful hyperthermia to destroy cancer cells. The temperature enlargement is noticed in Fig. 3(b) according to the rise in the thermal slipping at walls, which enhances the temperature gradient at the thermal boundary layer. Moreover, the nanofluid thermal conductivity was enhanced by increasing the nanoparticles' volume fraction. This improvement leads to effective heat dissipation and increases heat transfer efficiency to the tumors, reducing the temperature profiles of the nanofluid, as shown in Fig. 3(c). This decay in the temperature occurs due to the conversion of heat energy to kinetic energy and the low viscosity of the nanofluid. The thermal radiation parameter $R_{\rm p}$ is responsible for the heat production rate due to the viscous dissipation effect and its conversion to heat generation. This effect is observed in Fig. 3(d) with higher temperature profiles for thermal slipping conditions.

Table 4. The Sundry emerging physical parameters corresponding to Figs. 3(a)–3(d).

Physical parameters / Figures	$P_{\rm a}$	$P_{\rm e}$	β	γ	$K_{\rm nf}/K_{\rm f}$	$R_{\rm p}$	$R_{\rm l}$
Figure 3(a)	1	0.01	0.1 0.2 0.3 0.4	0.1	200	0.2	0.1
Figure 3(b)	1	0.01	0.1	0 0.1 0.2 0.3	200	0.2	0.1
Figure 3(c)	1	0.01	0.1	0.1	100 200 300 400	0.2	0.1
Figure 3(d)	1	0.01	0.1	0.1	200	0.2 0.4 0.6 0.8	0.1

The data corresponding to Figs. 3(a)–3(d) are tabulated in Table 4. Specifically, the influence of thermal radiation is discussed in the context of viscous dissipation and energy conversion mechanisms. When radiation effects are significant, the absorbed electromagnetic energy is converted into internal energy, increasing the local thermal energy of the nanofluid. This is particularly evident under thermal slip conditions at the boundaries, where temperature gradients at the wall are amplified, as demonstrated in Fig. 3(d).

This mechanism enhances localized hyperthermia, which is beneficial for targeted cancer treatment through thermal ablation. Moreover, the impact of nanoparticle volume fraction on the effective thermal conductivity is clarified using classical nanofluid theory. The introduction of high-conductivity nanoparticles into the base fluid increases the heat conduction pathways, thus improving the fluid's ability to transfer thermal energy. However, the observed temperature reduction in Fig. 3(c) is attributed to enhanced convective transport and reduced fluid viscosity, which allows kinetic energy to dominate, in line with the energy conversion model for low-viscosity nanofluids. Additionally, we have elaborated on the role of the internal heat generation parameter β and the thermal slip parameter γ in Figs. 3(a) and 3(b). Internal heat generation raises the core temperature of the fluid, simulating a scenario of active metabolic or therapeutic heating. At the same time, thermal slip alters the boundary-layer behavior, affecting the near-wall thermal gradient and enhancing surface heat transfer. Collectively, these insights illustrate a complex coupling between electromagnetic, thermal, and fluidic forces, all of which are crucial for designing efficient nanofluid-based biomedical treatments. These results agree with the outcomes of Adnan and Ashraf.[53]

Figures 4(a)–4(d) illustrate the through-flow velocity profiles at the preamble glial boundary layer. This velocity indicates the leakage rate of nanofluid in the radial direction. Figure 4(a) demonstrates that the increase in the magnetic field reduces the glial preamble area and restricts the leak velocity. Figure 4(b) presents the same inversely proportional effect on the through-flow velocity due to the increase in gold AuNPs volume fraction. The higher volume fraction concentration increases fluid viscosity and reduces flow velocity due to intensification in nanoparticle wall interactions. Figure c reveals that the increase in brain tissue permeability ($M_{\rm e}$) boosts

the leaking of nanofluid near brain tissue, consequently raising the through-flow velocity. The increase in the elastic brain tissue deformation enlarges the porous area of the preamble glial boundary layer and enhances the throughflow velocity, as shown in Fig. 4(d). The data corresponding to Figs. 5(a)–5(d) are tabulated in Table 5.

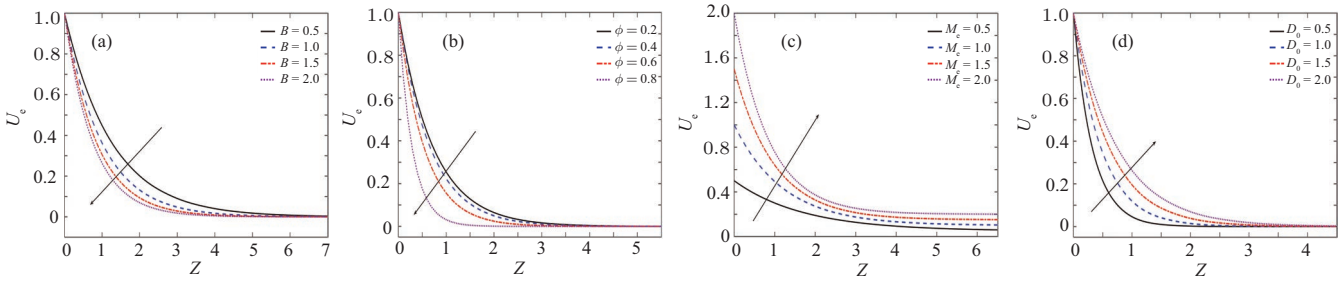


Fig. 4. The through-flow velocity of the nanofluid at the glial boundary versus the axial direction: (a) the magnetic flux intensity effect, (b) the volume fraction concentration of nanoparticles effect, (c) the permeability of brain tissue effect, and (d) the deformation of brain tissue effect.

Table 5. The Sundry emerging physical parameters corresponding to Figs. 4(a)–4(d).

Physical parameters / Figures	R_1	E_e	B	ϕ	M_e	D_0	P_e	P_a	L
Figure 4(a)	0.1	0.2	0.5 1 1.5 2.0	0.1	1	1.5	0.01	1	10
Figure 4(b)	0.1	0.2	1	0.2 0.4 0.6 0.8	1	1.5	0.01	1	0.5
Figure 4(c)	0.1	0.2	1	0.1	0.5 1 1.5 2.0	1.5	0.01	1	0.5
Figure 4(d)	0.1	0.2	1	0.1	1	0.5 1 1.5 2.0	0.01	1	0.5

Figures 5(a)–5(d) highlight the pressure distribution along the streamwise direction. Figure 5(a) illustrates the augmentation of the magnetic field reduces total energy and pressure distribution. Figure 5(b) shows that the increasing volume fraction of nanoparticles leads to a decrease in the pressure distribution as it enhances the fluid viscosity and resistance to flow, reducing the nanofluid pressure along the streamwise direction. Conversely, in Fig. 5(c), the increase in brain tissue permeability (M_e) results in boosting the leaking of nanofluid at brain tissue, consequently reducing the pressure. In contrast, the increase in the elastic brain tissue deformation improves the pressure of the nanofluid, as illustrated in Fig. 5(d). The data corresponding to Figs. 5(a)–5(d) are listed in Table 6.

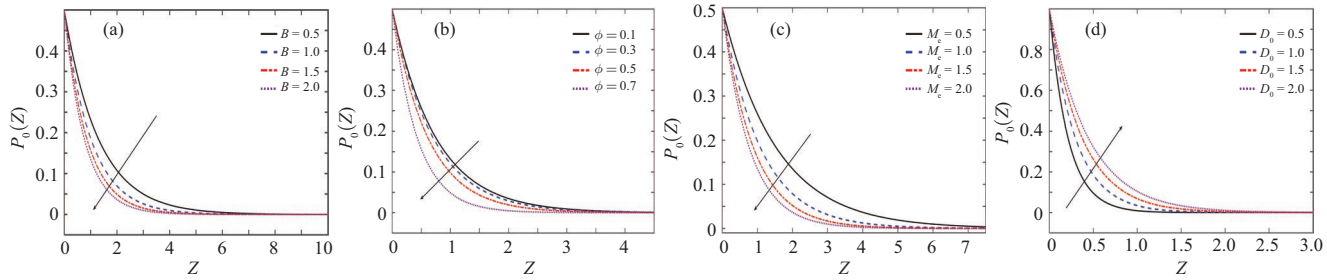


Fig. 5. The pressure distribution of the nanofluid *versus* the axial direction: (a) the magnetic flux intensity effect, (b) the volume fraction concentration of nanoparticles effect, (c) the permeability of brain tissue effect, and (d) the deformation of brain tissue effect.

The pressure gradient $(\mathrm{d}P_0/\mathrm{d}Z)$ distributions of the nanofluid flow under the influences of (B, ϕ, D_0, M_e) are included in Figs. 6(a)–6(d). Figure 6(a) displays that the pressure gradient increases by increasing the length of PVS. Notably, for a short length of PVS $(0 \leq z \leq 1.28)$, the augmentation in the Hartmann number reduces the pressure gradient. Also, it becomes more negative, which means normal streaming and assists the flow velocity. In contrast, for long lengths of PVS $(z > 1.28)$, the increase of magnetic field boosts the chances of the reversal flow corresponding to a positive pressure gradient, which resists the flow and reduces the average kinetic energy of the nanofluid streaming. Remarkably, the positive pressure gradients are not reached for the present condition, and the backflow does not occur. The explanation of these phenomena occurs according to the following analysis. When a magnetic field is applied perpendicular to an electrically conducting nanofluid, the Lorentz force arises due to the interaction between the induced electric currents in the fluid and the magnetic field. This force acts as an additional damping resistance opposing the motion of the fluid. In the initial short segment of the PVS $(0 \leq z \leq 1.28)$, the applied magnetic field tends to suppress fluctuations and streamline instabilities, thereby reducing the local flow resistance. This suppression leads to a more negative pressure gradient, which as-

sists flow development in the axial direction. However, in the longer segments ($z > 1.28$), the Lorentz force becomes dominant and acts significantly against the flow direction, requiring a larger positive pressure gradient to maintain momentum balance. This transition reflects a shift in the flow regime from magnetically assisted streaming to magnetically resisted flow. Nevertheless, under the present parameter conditions, the pressure gradient remains negative overall, indicating that backflow does not occur, though it is approached asymptotically. The same effect on the pressure gradient occurs in the case of increasing the permeability parameter of the glial boundary layer, as demonstrated in Fig. 6(c).

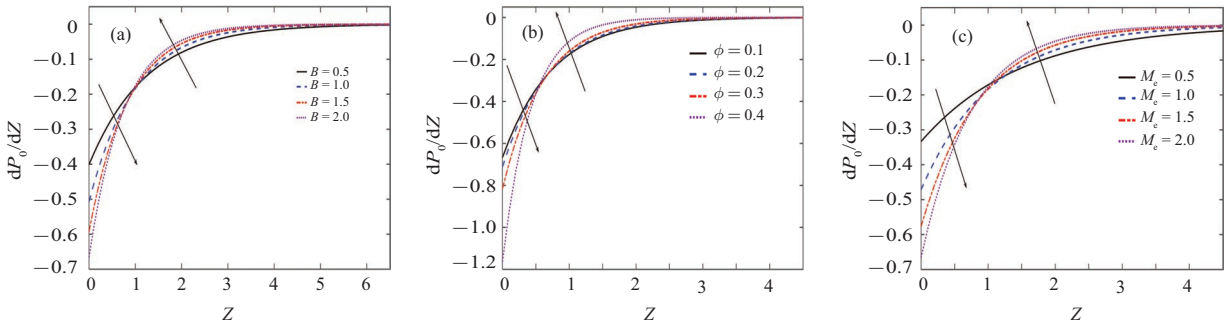


Fig. 6. The pressure gradient of the nanofluid *versus* the axial direction: (a) the magnetic flux intensity effect, (b) the volume fraction concentration of nanoparticles' effect, and he permeability of brain tissue effect.

Table 6. The Sundry emerging physical parameters corresponding to Figs. 5(a)–5(d).

Physical parameters / Figures	R_1	B	ϕ	M_e	D_0	P_e	P_a	L
Figure 5(a)	0.1	0.5 1.0 1.5 2.0	1	0.5	1.5	0.01	0.5	10
Figure 5(b)	0.1	1	0.1 0.3 0.5 0.7	0.5	1.5	0.01	0.5	10
Figure 5(c)	0.1	1	1	0.5 1.0 1.5 2.0	1.5	0.01	0.5	10
Figure 5(d)	0.1	1	1	0.5	0.5 1.0 1.5 2.0	0.01	0.5	10

The permeability of the glial boundary affects how fluid penetrates or interacts with the porous boundary layer. Higher permeability lowers wall resistance, effectively allowing more mass transport across the boundary. From a microscopic perspective, this alters the hydraulic resistance and boundary layer thickness, resulting in a modified axial pressure distribution. Similar to the magnetic field, increasing D_0 tends to reduce the axial resistance initially (short PVS length) but requires a higher pressure gradient downstream to compensate for altered flow behavior due to boundary-layer interactions. The nanoparticle concentration effect is also incorporated in Fig. 6(b).

For the short length of PVS ($0 \leq z \leq 0.52$), increasing (ϕ) means more viscosity and less nanofluid velocity, and to maintain the same flow rate, the pressure gradient must decrease because the flow resistance has increased due to the increased (ϕ). The decrease in the pressure gradient adjusts to balance this resistance. This effect is reversed in the case of long lengths of PVS ($z > 0.52$) because the flow has a transition to a more stable and fully developed regime, wherein the effects of viscosity are less dominant, and the pressure gradient increases to maintain the flow rate where the momentum of the nanofluid becomes more significant. Adding nanoparticles to the base fluid increases effective viscosity and thermal conductivity. Microscopically, nanoparticles disturb the local fluid layers, increasing intermolecular friction and momentum diffusion. In the short PVS region ($0 \leq z \leq 0.52$), the rise in viscosity leads to increases in the resistance to flow. Consequently, to maintain a constant flow rate, the pressure gradient must decrease, aligning with the principles of viscous drag compensation in laminar flow. In contrast, for longer segments ($z > 0.52$), the flow transitions toward a fully developed regime where inertial effects become more significant and the relative influence of viscosity diminishes. Here, the pressure gradient increases to sustain momentum transport through the nanofluid column, illustrating a nonlinear interplay between viscosity enhancement and momentum dominance. The data corresponding to Figs. 6(a)–6(c) are provided in Table 7.

Figures 7(a)–7(e) indicate the deformation of the glial permeable brain tissue corresponding to axial flow direction under the external effects of transversal magnetic field (B), pressure in the brain tissue (P_e), stiffness of brain tissue (E_e), and brain tissue permeability (M_e). All these aforementioned factors are causing a reduction in brain tissue deformability, as investigated in Figs. 7(a)–7(d). The data corresponding to Figs. 7(a)–7(d) are listed in Table 8.

Table 7. The Sundry emerging physical parameters corresponding to Figs. 6(a)–6(d).

Physical parameters / Figure	L	P_a	B	ϕ	M_e	R_1	P_e
Figure 6(a)	4	0.5	0.5 1.0 1.5 2.0	0.1	1	0.1	0.01
Figure 6(b)	4	0.5	1	0.1 0.2 0.3 0.4	1	0.1	0.01
Figure 6(c)	4	0.5	1	0.1	0.5 1.0 1.5 2.0	0.1	0.01

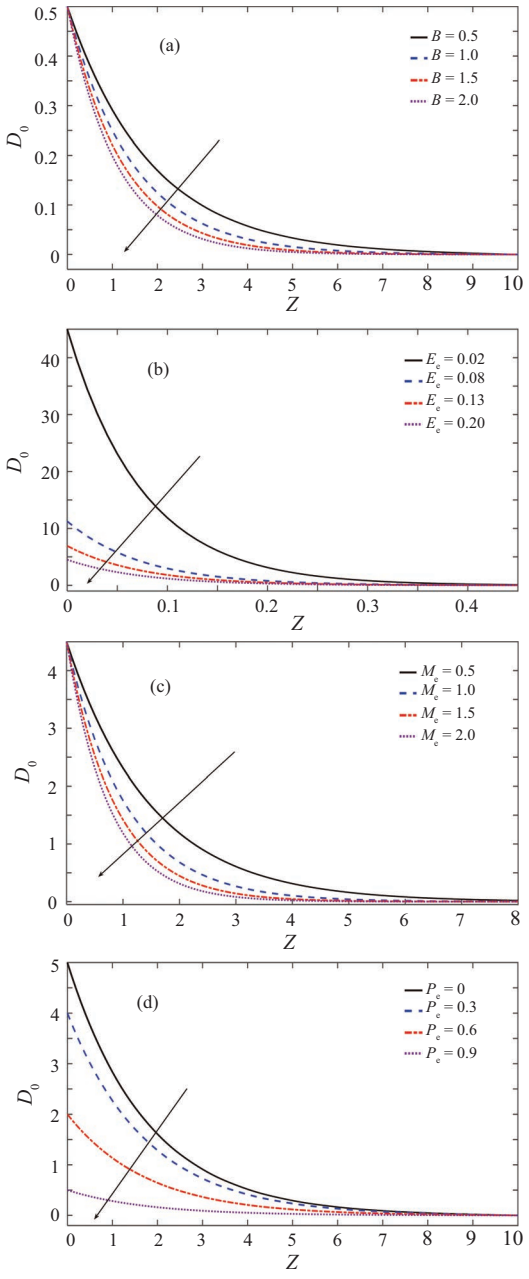


Fig. 7. The deformation of the glial permeable brain tissue *versus* the axial direction: (a) the magnetic flux intensity effect, (b) the stiffness of brain tissue effect, (c) the permeability of brain tissue effect, and (d) the pressure of brain tissue effect.

Table 8. The Sundry emerging physical parameters corresponding to Figs. 7(a)–7(d).

Physical parameters / Figure	L	P_a	B	E_e	M_e	P_e	R_1
Figure 7(a)	10	1	0.5 1.0 1.5 2.0	0.2	1	0.1	0.1
Figure 7(b)	10	1	1	0.02 0.08 0.13 0.20	1	0.1	0.1
Figure 7(c)	10	1	1	0.2	0.5 1.0 1.5 2.0	0.1	0.1
Figure 7(d)	10	1	1	0.2		0 0.3	0.1

5. Conclusion

The detailed graphical analysis in this investigation elucidates key aspects concerning the interactions among the transverse magnetic field, hyperthermia heat source, thermal heat radiation, thermal slipping at the boundaries, and nanoparticles' concentrations on the performance of gold blood nanofluid during peristaltic flow. These insights are helpful for understanding how these parameters influence the streamwise and leak velocity, pressure gradient, and temperature distribution of the nanofluid through the PVS. This analysis is essential for evaluating process efficiency. The governing equations are solved following the procedures of the perturbation strategy. The effect of the Maxwell model for nanofluid thermal conductivity is also incorporated. Below are the critical remarks derived from the analyses.

(i) The net streamwise velocity of the nanofluid is significantly reduced by augmentation in Hartmann number due to the resistive action of Lorentz force related to the magnetic field strength.

(ii) Higher concentrations of nanoparticles increase the viscosity of the nanofluid due to internal friction, leading to a loss of average kinetic energy and reduced momentum transfer between nanofluid layers, thus reducing streamwise velocity.

(iii) The increase in thermal slipping enhances the thermal gradient at the boundary layers, boosting nanofluid momentum and increasing net axial velocity.

(iv) The rise of heat source intensity results in internal hyperthermia that enhances thermal buoyancy forces that directly accelerate fluid flow by increasing the nanofluid kinetic energy and streamwise velocity.

(v) The increase in heat source intensity enhances internal hyperthermia, which accelerates fluid flow and increases the kinetic energy of the nanofluid.

(vi) The increase in thermal slipping at the walls enhances the temperature gradient at the thermal boundary layer, thereby improving the thermal conductivity of the nanofluid.

(vii) Increasing the volume fraction of nanoparticles

ameliorates the thermal conductivity of the nanofluid, leading to improved heat dissipation and increased heat transfer efficiency to tumors.

(viii) The thermal radiation enhances the heat production rate through viscous dissipation and results in higher temperature profiles.

(xi) An increase in the magnetic field strength reduces the glial preamble area, which restricts the leakage velocity of the nanofluid in the radial direction, leading to lower flow rates.

(xii) Higher concentrations of AuNPs result in increased fluid viscosity, which negatively affects the flow due to intensified interactions at the nanoparticle wall.

(xiii) Stronger magnetic fields reduce total energy and pressure distribution in the nanofluid.

(ix) The pressure gradient of nanofluid flow changes with the length of the PVS, shorter lengths exhibit a decrease in pressure gradient with the increased magnetic field, whereas longer lengths can lead to flow resistance and reduced energy.

(x) The concentration of nanoparticles impacts viscosity at short PVS lengths, higher concentration leads to lower flow velocity and pressure gradient, but at longer lengths, the flow stabilizes and increases the pressure gradient to maintain the flow rate.

Acknowledgement

Sara Abdelsalam expresses her deep gratitude to Fundación Mujeres por África for supporting this work through the fellowship awarded to her.

References

[1] Davis M E 2016 *Clin. J. Oncol. Nurs.* **20** S2
[2] Kumar A, Ahlawat W, Kumar R and Dilbaghi N 2017 *Adv. Funct. Mater.* **27** 1700489
[3] Silva G A 2006 *Nat. Rev. Neurosci.* **7** 65
[4] Palaniyappan R, Kumar P M, Tamilarasan R and Suresh S 2024 *Indian J. Pharm. Educ. Res.* **58** S1185
[5] Gayathri R *Advancements in the Controlled Delivery of Nanodrugs to the Central Nervous System: Challenges and Innovations* (in press)
[6] Shabani L, Abbasi M, Azarnew Z, Amani A M and Vaez A 2023 *Biomed. Eng. Online* **22** 1
[7] Joshi R, Kumar P M, Tamilarasan R and Suresh S 2023 *J. Drug Deliv. Sci. Technol.* 105067
[8] Abdelsalam S I, Abdelwahab E T, Eldesoky I, Abumandour R M and Ahmed M 2025 *Acta Mech. Sin.* **41** 724077
[9] Abumandour R M, Eldesoky I M, Abdelwahab E T and Ahmed M M 2024 *Z. Angew. Math. Mech.* **104** e202300260
[10] Choi S U and Eastman J A 1995 *Enhancing Thermal Conductivity of Fluids with Nanoparticles* (Argonne National Laboratory)
[11] Kumar P M, Kumar J, Tamilarasan R, Sendhilnathan S and Suresh S 2015 *Eng. J.* **19** 67
[12] Dreaden E C, Mackey M A, Huang X, Kang B and El-Sayed M A 2011 *Chem. Soc. Rev.* **40** 3391
[13] Dreaden E C, Austin L A, Mackey M A and El-Sayed M A 2012 *Ther. Deliv.* **3** 457
[14] Mekheimer K S, Hasona W, Abo-Elkhair R and Zaher A 2018 *Phys. Lett. A* **382** 85
[15] Abdelsalam S I and Bhatti M 2019 *Sci. Rep.* **9** 260
[16] Zhu W, Li Y, Zhang L and Wang J 2024 *Crit. Rev. Oncol. Hematol.* 104541
[17] Bastiancich C, Da Silva A and Estéve M A 2021 *Front. Oncol.* **10** 610356
[18] Skandalakis G P, Rivera D R, Rizea C D and Bouras A 2020 *Int. J. Hyperthermia* **37** 3
[19] Abdelsalam S I, Magesh A, Tamizharasi P and Zaher A 2024 *Int. J. Numer. Methods Heat Fluid Flow* **34** 408
[20] Tharwat E, Magdy M, Eldesoky I M and Abumandour R M 2023 *Eng. Res. J.* **46** 555
[21] Magdy M, Abumandour R, Eldesoky I and Alotaibi H 2024*Mathematics* **12** 2024
[22] Nuwairan M A and Souayeh B 2022 *Micromachines* **13** 374
[23] Alqarni A J, Abo-Elkhair R, Elsaid E M, Abdel-Aty A H and Abdel-Wahed M S 2023 *Eur. Phys. J. Plus* **138**
[24] Hasona W, Almalki N, ElShekhipy A and Ibrahim M 2019 *Heat Transf. Asian Res.* **48** 938
[25] Ramki R and Lakshminarayana P 2024 *Mod. Phys. Lett. B* 2550043
[26] Venugopal Reddy K, Makinde O D and Gnaneswara Reddy M 2018 *Indian J. Phys.* **92** 1439
[27] Maier-Hauff K, Rothe R, Scholz R, Gneveckow U and Wust P 2011 *J. Neurooncol.* **103** 317
[28] van Landeghem F K, Maier-Hauff K, Jordan A and Hoffmann K T 2009 *Biomaterials* **30** 52
[29] Laurent S, Forge D, Port M, Roch A and Vander Elst L 2008 *Chem. Rev.* **108** 2064
[30] Hayat T, Tanveer A, Yasmin H and Alsaedi A 2014 *Appl. Bionics Biomech.* **11** 221
[31] Shaaban A A and Abou-Zeid M Y 2013 *Math. Probl. Eng.* **2013** 819683
[32] Srivastava V and Saxena M 1995 *Rheol. Acta* **34** 406
[33] Dimitropoulos C D, Edwards B J, Chae K S and Beris A N 1998 *J. Comput. Phys.* **144** 517
[34] Eytan O, Jaffa A J and Elad D 2001 *Med. Eng. Phys.* **23** 475
[35] Eldesoky I, Abumandour R, Kamel M and Abdelwahab E 2021 *Int. J. Appl. Comput. Math.* **7**
[36] Eldesoky I M, Abumandour R M and Abdelwahab E T 2019 *Z. Naturforsch. A* **74** 317
[37] Eldesoky I, Abumandour R, Kamel M and Abdelwahab E 2019 *SN Appl. Sci.* **1** 1
[38] Lakshmi R and Kavitha A 2024 *Int. J. Mod. Phys. B* **38** 2450212
[39] Abumandour R M, Eldesoky I M and Abdelwahab E T 2020 *Eng. Res. J.* **43** 231
[40] Zhang T T, Li W, Meng G, Wang P and Liao W 2016 *Biomater. Sci.* **4** 219
[41] Meng Q, Wang Y, Chen Y and Li W 2022 *J. Mater. Chem. B* **10** 271
[42] Romanó F, Suresh V, Galie P A and Grotberg J B 2020 *Sci. Rep.* **10** 21065
[43] Oraki Kohshour M, Papiol S, Delalle I, Rossner M J and Schulze T G 2023 *Eur. Arch. Psychiatry Clin. Neurosci.* **273** 1279
[44] Thomas J H 2019 *J. R. Soc. Interface* **16** 20190572
[45] Sweetman B and Linninger A A 2011 *Ann. Biomed. Eng.* **39** 484
[46] Kelley D H 2021 *Phys. Rev. Fluids* **6** 070501
[47] Bloomfield I, Johnston I and Bilston L 1998 *Pediatr. Neurosurg.* **28** 246
[48] Abbas Z, Rafiq M, Alshomrani A and Ullah M 2021 *Case Stud. Therm. Eng.* **23** 100817
[49] Akbar N S and Butt A W 2016 *Appl. Nanosci.* **6** 379
[50] Yu W and Choi S U S 2003 *J. Nanopart. Res.* **5** 167
[51] Hussain A, Malik M Y, Salahuddin T and Rubab A 2022 *Appl. Sci.* **12** 1601
[52] Wang P and Olbricht W L 2011 *J. Theor. Biol.* **274** 52
[53] Adnan and Ashraf W 2022 *Adv. Mech. Eng.* **14** 16878132221106577